PHOTONICS Research

Optically induced atomic lattice with tunable near-field and far-field diffraction patterns

Feng Wen,[1,2,†] Huapeng Ye,[2,†] Xun Zhang,[1] Wei Wang,[1] Shuoke Li,[1] Hongxing Wang,[1,*] Yanpeng Zhang,[1] and Cheng-wei Qiu[2]

[1]Key Laboratory for Physical Electronics and Devices of the Ministry of Education & School of Science & Shaanxi Key Laboratory of Information Photonic Technique & Institute of Wide Bandgap Semiconductors, Xi'an Jiaotong University, Xi'an 710049, China
[2]Department of Electrical and Computer Engineering, National University of Singapore, 4 Engineering Drive 3, Singapore 117583, Singapore
*Corresponding author: hxwangcn@mail.xjtu.edu.cn

Received 11 August 2017; revised 3 October 2017; accepted 4 October 2017; posted 5 October 2017 (Doc. ID 304051); published 8 November 2017

Conventional periodic structures usually have nontunable refractive indices and thus lead to immutable photonic bandgaps. A periodic structure created in an ultracold atoms ensemble by externally controlled light can overcome this disadvantage and enable lots of promising applications. Here, two novel types of optically induced square lattices, i.e., the amplitude and phase lattices, are proposed in an ultracold atoms ensemble by interfering four ordinary plane waves under different parameter conditions. We demonstrate that in the far-field regime, the atomic amplitude lattice with high transmissivity behaves similarly to an ideal pure sinusoidal amplitude lattice, whereas the atomic phase lattices capable of producing phase excursion across a weak probe beam along with high transmissivity remains equally ideal. Moreover, we identify that the quality of Talbot imaging about a phase lattice is greatly improved when compared with an amplitude lattice. Such an atomic lattice could find applications in all-optical switching at the few photons level and paves the way for imaging ultracold atoms or molecules both in the near-field and in the far-field with a nondestructive and lensless approach.

OCIS codes: (050.0050) Diffraction and gratings; (270.1670) Coherent optical effects; (050.5080) Phase shift; (070.6760) Talbot and self-imaging effects.

https://doi.org/10.1364/PRJ.5.000676

1. INTRODUCTION

In the past few years, artificial periodic structures, such as photonic crystals [1–5] and metamaterials [6–9], have attracted increasing attention due to their unprecedented capacities of engineering the transmission and reflection properties of waves. An important property of such applications is the ability to strongly modify the propagation of light in certain directions and frequencies. A number of new physical phenomena have been predicted to occur in these materials, including strong localization of light [10], inhibited spontaneous emission from atoms [11], photon–atom bound states [11], all-optical signal processing, and switching [12].

Conventionally, photolithography and electron beam lithography are widely used to fabricate the periodic structures with microsized or nanosized features. However, the refractive index of the resulting periodic structures is usually nontunable, thus leading to immutable photonic bandgap (PBG). To fully explore the potential of photonic crystals, it is crucially important to achieve a dynamical tunability of their bandgap [13]. In previous studies, a distinct approach to generate spatially periodic structures, based on the electromagnetically induced grating (EIG) [14], is proposed by Ling *et al.* [15] and experimentally demonstrated in cold [16] and hot [17] atomic samples. Very recently, the spatially dependent electromagnetically induced transparency (EIT) in cold atoms was demonstrated by using the phase profile as a control parameter for the atomic opacity [18]. Unlike traditional photonic crystals, here a periodic structure is created by externally controlled light, and a novel photonic structure with an optically tunable PBG is achieved [19]. The EIG with tunable first-order diffraction has attracted considerable interest due to its potential applications in all-optical switching and routing [17], light storage [20], probing optical properties of materials [21], optical bistability [22], shaping a biphoton spectrum [23], and beam splitting and fanning [24]. However, 2D EIG and its diffraction pattern in near-field and far-field have not been demonstrated yet. In this paper, we demonstrate that optical lattices resulting from amplitude modulation and phase modulation can be realized in an ultracold atoms ensemble by interfering four ordinary plane waves under different parameter conditions. We analyze

theoretically the families of such optically induced square lattices and then discuss the corresponding diffraction pattern both in near-field and far-field regions. We identify that the phase modulation plays a significant role not only in the efficiency of diffracting light into high-order directions but also in the improvement of the quality of the Talbot carpet pattern (visibility and the signal-to-noise ratio). This work may offer a nondestructive and lensless way to image ultracold atoms or molecules both in the near-field and in the far-field.

It is worth mentioning that our system has the following advantages. First, the optical lattice written in an atomic assemble is reconfigurable and can be dynamically tuned, leading the refractive index change, and the PBG structures of our scheme are sensitive to the adjusting the frequency detuning, so the transmission and reflection of the propagating light can be dynamically modulated. Further detailed studies of these effects will be presented elsewhere. Second, using the multibeam interference method, other complex lattice structures, i.e., quasi-crystals, kagome lattice, defect mediated lattice, honeycomb lattice, Bessel lattice, virtual lattice, ring lattice, and 3D photonic lattice, can all be realized in current systems. Third, formation of the lattice, as well as the tuning, is all done all optically.

2. THEORETICAL MODEL

The scheme to construct optically induced square lattices relies on periodically manipulating the refractive index of an ultracold atoms (or molecules) ensemble. As illustrated in Fig. 1(a), our model consists of four strong control fields of frequency ω_C and wave number k_C, a weak probe field of frequency ω_P and wave number k_P, and an ensemble of closed three-level cascade-type ultracold atoms (or molecules) composing of a ground state $|a\rangle$, a metastable state $|b\rangle$, and an excited state $|c\rangle$. The metastable state $|b\rangle$ is coupled to the excited state $|c\rangle$ via the four strong control fields near resonance on the $|b\rangle \rightarrow |c\rangle$ transition, while the $|a\rangle \rightarrow |b\rangle$ transition is connected by the probe beam with Rabi frequency Ω_P.

The four controlling plane waves, which are injected into the atomic sample and interact with the atomic ensemble by coupling the atomic transition $|b\rangle \rightarrow |c\rangle$, are the lattice-forming lasers. To be specific, two plane waves being symmetrically displaced with respect to the z axis are incident upon the atomic sample at a small angle θ, whose intersection will generate a standing wave along the x direction within the atomic ensemble. In the same way, another two plane waves generate a standing wave along the y direction inside the medium. The effective Rabi frequency of the four strong controlling fields can be written as $|G_{\text{eff}}(x,y)|^2 = |\Omega_C \sin(\pi x/a)|^2 + |\Omega_C \sin(\pi y/b)|^2$. Here, Ω_C is the Rabi frequency of one of the four controlling fields and assumed to be real for simplicity. a (b) is the spatial period along the X (Y) direction [see Fig. 1(b)], which can be made arbitrarily larger than the wavelength of the controlling fields by varying θ. A 2D optically induced lattice will be produced within the ultracold atoms (or molecules) ensemble if the condition $\Omega_C \gg \Omega_P$ is satisfied. Two points should be emphasized herein. First, the stability of the optically induced lattice structure is determined by lattice-forming beams. As long as the laser beams forming the optical lattice are stable, small fluctuations should not affect our main results. Second, by employing two-photon Doppler-free configurations in the thermal atomic vapor, our scheme could be realized in the thermal atomic vapor.

Spanning the Hilbert space with bare states ($|a\rangle$, $|b\rangle$, and $|c\rangle$) and applying the rotational wave approximation, the Hamiltonian in the interaction picture can be represented by ($\hbar = 1$)

$$H = G_P e^{-i\Delta_P t}|a\rangle\langle b| + G_{\text{eff}} e^{-i\Delta_2 t}|b\rangle\langle c| + \text{h.c}, \quad (1)$$

where μ_{ij} is the electric dipole matrix element to atomic transition $|i\rangle \rightarrow |j\rangle$ ($i, j = a, b, c$). $\Delta_1 = \omega_P - \omega_{ba}$ and $\Delta_2 = \omega_C - \omega_{bc}$ are single photon frequency detunings of E_P and $E_{\text{eff}}(x, y)$ from

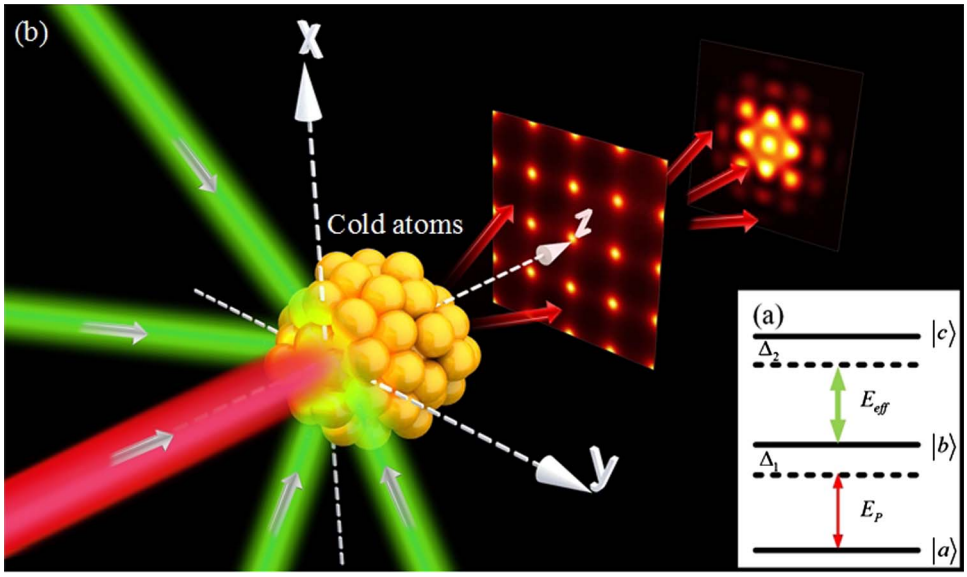

Fig. 1. (a) Cascade-type three-level scheme with $|a\rangle$ [$5S_{1/2}(F = 3)$], $|b\rangle$ [$5P_{3/2}(F = 3)$], and $|c\rangle$ ($5D_{5/2}$) of ^{85}Rb atoms [25], interacting with three laser beams: probe field E_P and two lattice-forming fields $E_2(x)$ and $E_3(y)$. (b) The geometry of four laser beams applied upon a cold atoms ensemble along the z direction, and the corresponding near-field and far-field diffraction patterns of a probe field.

the transitions $|a\rangle \rightarrow |b\rangle$ and $|b\rangle \rightarrow |c\rangle$, respectively, with $\omega_{ij} = \omega_i - \omega_j$ $(i, j = a, b, c)$. From dressed state theory analysis, the atomic transition channel $|b\rangle \rightarrow |c\rangle$ is periodically dressed by $E_{\text{eff}}(x, y)$, and then $|b\rangle$ will be split into dressed states $|+\rangle$ and $|-\rangle$, with eigenvalues $\lambda_{\pm} = \Delta_2/2 \pm (\sqrt{\Delta_2^2/4 + |G_{\text{eff}}(x,y)|^2}$. Eventually, 2D square lattice states $|\pm\rangle$ are formed in space.

The induced polarization at ω_P is $P(\omega_P) = \varepsilon_0 \chi(\omega_P) E_P(\omega_P)$, and the optically induced susceptibility can be expressed as

$$\chi = \frac{iN|\mu_{ab}|^2}{2\hbar\varepsilon_0} \frac{\gamma_{ac} - i\Delta_{12}}{G_{\text{eff}}^2(x) + (\gamma_{ab} - i\Delta_1)(\gamma_{ac} - i\Delta_{12})}, \quad (2)$$

where $\Delta_{mn} = \Delta_m - \Delta_n$ is two-photon detuning, N the atomic ensemble density, ε_0 the vacuum permittivity, and γ_{ij} the dephasing rate between $|i\rangle$ and $|j\rangle$.

As the lattice-forming laser has an amplitude and space period, as shown in Fig. 2(a), the optically induced polarization χ at the probe frequency ω_P is periodically modulated by $E_{\text{eff}}(x, y)$. To illustrate explicitly this point, in Figs. 2(b) and 2(c), we compare the optical properties of the probe field at the nodes and antinodes of the optically induced nonmaterial lattice. From the absorption curve [solid lines in Figs. 2(b) and 2(c)], it is found that the probe field is absorbed strongly at the nodes and almost transmitted at the antinodes. This can lead to a substantial amplitude modulation across the probe beam. On the other hand, the dispersion within the EIT [14] window [dashed line in Figs. 2(b) and 2(c)] is positive to the probe field at the nodes but negative at the antinodes. This feature may open the possibility of a large phase modulation across the probe beam.

Since the absorption and dispersion coefficients of the probe field highly depend on $E_{\text{eff}}(x, y)$, they are expected to change periodically as the lattice-forming laser changes from nodes to antinodes across the x axis and the y axis. Therefore, the 2D spatially periodic amplitude and phase modulation are realized when the probe field passes through the optically induced lattice region along the z axis. The dynamics of the probe field in such a lattice is described by Maxwell's wave equation, and here the optically induced polarizations serve as the driving source. Under the slowly varying envelope approximation, a self-consistent equation for E_P becomes

$$\frac{\partial E_P}{\partial z} = (-\alpha/2 + i\sigma)E_P, \quad (3)$$

where $\alpha = (4\pi/\lambda)\text{Im}[\chi(\omega_P)]$ and $\sigma L = (2\pi L/\lambda)\text{Re}[\chi(\omega_P)]$, corresponding to the two-photon absorption coefficient and the phase shift of the probe laser, respectively, are functions of x and y. Equation (3) can be solved analytically, and the normalized transmission function with interaction length L is

$$T(x, y) = \exp\left[-\frac{\alpha(x, y)L}{2} + i\sigma(x, y)L\right]. \quad (4)$$

In the following, the propagation dynamics of such optically induced lattice will be derived, and then the corresponding diffraction pattern in two limiting regimes, namely, the near-field and far-field regimes, will be presented. In the near-field regime (or Fresnel near-field regime) where the diffraction effects are negligible, we will propose a scheme to realize the self-imaging of ultracold atoms or molecules and demonstrate that the quality of imaging can be further improved in the current scheme. In the far-field (or Fraunhofer diffraction regime) where the diffraction spread is dominant, we will show how the novel properties of phase shift can help to effectively diffract light into the higher-order direction.

In the Fresnel near-field regime, using the Fresnel–Kirchhoff diffraction integral, the diffraction intensity distribution is proportional to

$$E(X, Y, Z) = \iint \text{d}x\text{d}y T(x, y) \exp\left[ik_P\left(2Z + \frac{x^2 + y^2}{2Z} - \frac{xX + yY}{2Z} + \frac{X^2 + Y^2}{2Z}\right)\right], \quad (5)$$

where x (y) is the transverse coordinate at the output surface of the atomic ensemble, and X (Y) at the imaging planes, and z is the diffraction distance from the atomic ensemble to

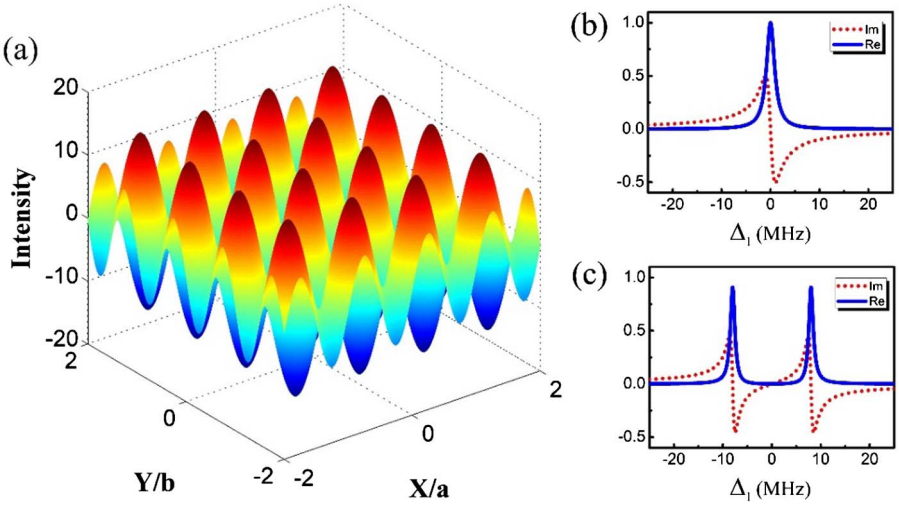

Fig. 2. (a) The periodical modulation of the lattice-forming laser due to the four-beam interference pattern with $\Omega_C = 8$ MHz. The absorption spectrum and dispersion spectrum (b) at the nodes and (c) the antinodes of the lattice-forming laser.

the observation plane. To solve the above integral, we expand $T(x,y)$ in Eq. (4) into a 2D Fourier series

$$T(x,y)=\sum_{m,n=-\infty}^{\infty} C_{mn}\exp\left[-i\left(\frac{2\pi m}{a}x+\frac{2\pi n}{b}y\right)\right], \quad (6)$$

where C_{mn} is a 2D Fourier coefficient. a and b are the spatial periods along the X and Y directions, respectively. By substituting Eq. (6) into Eq. (5), we recover the traditional Talbot effect

$$\Psi(u_1,u_2;v_1,v_2)=C_0\sum_{n=-\infty}^{\infty} c_{mn}\left\{\exp\left[-i\pi\lambda_P Z\left(\frac{m^2}{a^2}+\frac{n^2}{b^2}\right)\right]\times\exp\left[i2\pi\left(\frac{m}{a}X+\frac{n}{b}Y\right)\right]\right\}, \quad (7)$$

where the irrelevant terms have been absorbed into C_0. Some interesting conclusions can be immediately obtained from Eq. (7). First, the amplitude profile of the diffraction field matches with that at the output plane of the ensemble if all the diffraction orders are in the same phase. Hence, the imaging of atomic lattices can be recovered in those planes $z_T=m(a^2+b^2)/\lambda_P$, where m, denoting the order of self-imaging, is a positive integer. Second, the resolution of Talbot imaging is independent of the property of atomic lattices. Third, as the amplitude/phase information of the atomic lattices is contained in the 2D Fourier coefficient, the visibility and the signal-to-noise ratio of Talbot imaging can be modulated through the parameters of atomic lattices.

From Fraunhofer diffraction theory [26], the far-field diffraction pattern over the diffraction angle θ with respect to the z direction is proportional to the Fourier transform of $T(x,y)$ if the incident probe laser is a plane wave [15,27] The diffraction intensity distribution is given by

$$I(\theta_x,\theta_y)=|J(\theta_x,\theta_y)|^2\frac{\sin^2[P\pi a\ \sin\ (\theta_x/\lambda_P)]}{P^2\sin^2[\pi a\ \sin\ (\theta_x/\lambda_P)]}\times\frac{\sin^2[Q\pi b\ \sin\ (\theta_y/\lambda_P)]}{Q^2\sin^2[\pi b\ \sin\ (\theta_y/\lambda_P)]}, \quad (8)$$

where $J(\theta_x,\theta_y)=\iint \mathrm{d}x\mathrm{d}y T(x,y)\exp[-i2\pi x a\ \sin\ (\theta_x/\lambda_P)]\exp[-i2\pi y b\ \sin\ (\theta_y/\lambda_P)]$ represents the Fraunhofer diffraction of a single space period, and the diffraction efficiency into any diffraction-order along the x axis and the y axis is determined by $a\sin\theta_x=m\lambda_P$ and $b\sin\theta_y=n\lambda_P$, respectively. P and Q are the number of spatial periods along the x axis and the y axis of the lattices which are illuminated by the probe beam. θ_x (θ_y) is the diffraction angle with respect to x (y) direction.

3. RESULTS AND DISCUSSION

Using the equations outlined in Section 2, the near-field and far-field diffraction patterns of two typical atomic lattices will be discussed in this section. For the sake of convenience, we assume that the trapped ^{85}Rb atom cloud in a magneto-optical trap is about 1 mm in diameter, with the laser cooled to around 4.4 mK. The upper transition $|b\rangle\rightarrow|c\rangle$ $[5S_{1/2}(F=3)\rightarrow 5P_{3/2}(F=3)]$ is specifically derived by four elliptical Gaussian-shaped coupling beams, which are split from a CW Ti:sapphire laser with power of about p_{eff} 20 mW and a wavelength of $\lambda_{\mathrm{eff}}=775.98$ nm. Those four beams are symmetrically placed with respect to the z axis and intersect at the center of the rubidium cell at an angle of θ to establish an optical lattice in the transverse plane of the ^{85}Rb atom cloud, with lattice period $a=\lambda_{\mathrm{eff}}/(2\sin\theta)$ and $b=\lambda_{\mathrm{eff}}/(2\sin\theta)$ along directions x and y, respectively. Meanwhile, the probe field generated from an external cavity diode laser (with a wavelength of 780 nm and power of 5 mW) is partially overlapping with the four coupling beams and used to connect the lower transition $|a\rangle\rightarrow|b\rangle$ $[5P_{3/2}(F=3)\rightarrow 5D_{5/2}]$. We start from investigating the Fraunhofer diffraction patterns of optically induced lattice within a parameter regime of $\Delta_1=\Delta_2=0$.

Figures 3(a) and 3(b) show the transmission profiles over four space periods and the normalized Fraunhofer diffraction patterns, respectively. It can be found from Fig. 3(a) that the probe profile around the antinodes is almost without absorption but with strong absorption at the nodes. This atomic lattice tends to gather light to the center maximum and the higher-order diffraction patterns are almost invisible, as shown in Figs. 3(b) and 3(d). Therefore, a phenomenon reminiscent of the pure amplitude-type lattice is implemented in such an atomic lattice. This phenomenon coincides with our expectation. On one hand, because the intensity of the lattice-forming laser at the transverse locations around the nodes is very weak, the probe beam is absorbed according to the usual Beer law [see the solid line in Fig. 2(b)]. At the antinodes, however, the probe is absorbed much less due to the EIT effect [see the solid line in Fig. 2(c)]. This leads to a periodic amplitude modulation across the beam profile of the probe field. On the other hand, the real part of the susceptibility vanishes as $\Delta_1=0$, and the phase modulation is absent in such atomic lattices [see Fig. 3(c)]. Therefore, the higher-order diffraction obtained by this pure amplitude lattice is very limited.

Next, we optimize the parameter to create a phase modulation lattice, which is lossless and highly efficient in diffracting light into high-order directions. In order to realize this objective, the controlling fields should have a high intensity and resonance interaction with the transition $|b\rangle\rightarrow|c\rangle$ so that a good level of transparency across the beam profile can be well maintained. Meanwhile, the weak probe is optimized to tune away from the transition $|a\rangle\rightarrow|b\rangle$ but still operates within the EIT window to introduce a π phase modulation ($\sigma L=\pi$).

Figures 4(a) and 4(c) display the amplitude and phase of the transmission function $T(x,y)$ with settings $\Delta_1=10$ MHz, $\Delta_2=0$ MHz, and $\Omega_C=15$ over four space periods. Within a single space period, i.e., $(-0.5a\le x\le 0.5a$, $-0.5b\le y\le 0.5b)$, the antinode is located at $(x=0,\ y=0)$ and the node is located at $(x=\pm 0.5a,\ y=0)$ and $(x=0,\ y=\pm 0.5b)$. For a more intuitive display, the amplitude (solid curve) and phase (dashed curve) of the transmission function $T(x,y)$ in a 1D graph over a single period are presented in Fig. 4(c). A small absorption in the transmission and a relatively stable phase shift of $\pi/2$ can be observed around the antinodes of such lattice in Fig. 4, while a phase modulation of about $-\pi/2$ is introduced into the transmission profile at the nodes and the corresponding absorption intensity is about 49%. Moreover,

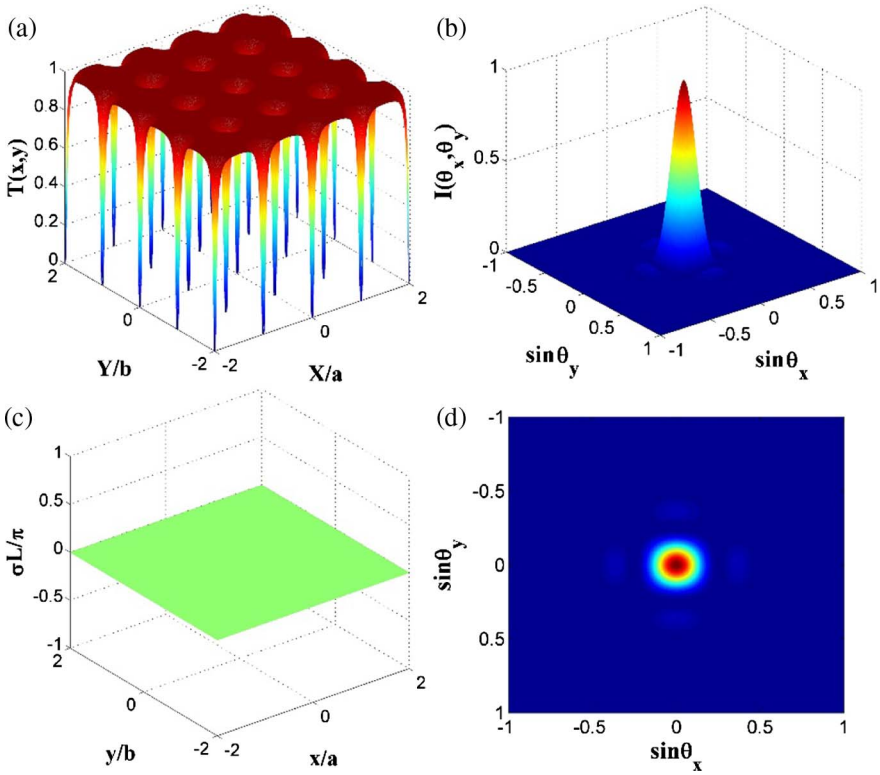

Fig. 3. Amplitude-type lattice, with settings $\Omega_C = 15$ MHz, $\Delta_1 = 0$ MHz, and $\Delta_2 = 0$ MHz. (a) The amplitude and (b) the phase of the transmission function $T(x, y)$ plotted over four space periods along x and y. (c) The corresponding normalized diffraction intensity $I(\theta_x, \theta_y)$ as a function of $\sin\theta_x$ and $\sin\theta_y$. (d) 2D transverse patterns corresponding to (c). Other parameters are $\gamma_{ab} = 1$ MHz, $\gamma_{ac} = 0.1$ MHz, $a/\lambda_P = b/\lambda_P = 4$, $L = 10$, and $P = Q = 1$.

both the absorption and phase experience rapid changes around $\|G_{\text{eff}}(x)\sin(\pi x)\| = \|\Delta_1\|$ and $\|G_{\text{eff}}(x)\sin(\pi y)\| = \|\Delta_1\|$. It can be seen in Figs. 4(b) and 4(d) that the amount of light diffracted into zero-order is completely converted into higher-order diffraction light, i.e., the first order along the x axis (or the y axis) or even first order in the four quadrants is considerably increased. In our model, although it is impossible to realize the ideal phase lattice, the resulting lattice possesses some features similar to the ideal phase lattice. First, the maximum absorption at the nodes is only 49%, while it is close to zero in the other regions of the single period, implying a low energy loss inside the atomic medium. Second, the phase difference between the nodes and the antinodes is of the order of π [see Fig. 4(e)].

In order to quantitively study the far-field intensity distribution of the amplitude lattice and the phase-type lattice, the intensity of different diffraction orders, including zero-order $I_P(\theta_x^0, \theta_y^0)$ (solid line), the first-order along the x axis $I_P(\theta_x^1, \theta_y^0)$ (dashed line), and the first-order in the four quadrants $I_P(\theta_x^1, \theta_y^1)$ (dashed–dotted line), are presented in Fig. 5. We first focus on the amplitude lattices with the parameters similar to Fig. 3. As shown in Fig. 5(a), both $I_P(\theta_x^1, \theta_y^0)$ and $I_P(\theta_x^1, \theta_y^1)$ increase almost linearly to a maximum value and then decrease with Ω_C. This can be interpreted by the following two reasons. On one hand, EIT will gradually open up the individual antinodes, making more light available for higher-order diffraction. One the other hand, if Ω_C is further increased, however, the majority part of one period of lattices is transparent. Such a wide opening period will limit the chances of light to stray into the higher order. In the absence of phase modulation, a small amount of energy is shifted into the higher order, about 0.98% with $I_P(\theta_x^1, \theta_y^0)$ and 0.18% with $I_P(\theta_x^1, \theta_y^1)$. However, $I_P(\theta_x^0, \theta_y^0)$ is still dominant and only the zero-order diffraction component is visible [see Figs. 3(a) and 5(a)], whereas the higher-order diffraction attainable by this pure amplitude lattice is very limited. Then, we turn to the case of phase lattices where the phase modulation is introduced with settings $\Delta_1 = 10$ MHz, $\Delta_2 = 0$ MHz. It can be observed from Fig. 5 that more energy of probe field is transferred from zero-order to higher-order directions in such phase lattice [as shown in Fig. 5(b)] than in the amplitude lattices [as shown in Fig. 5(a)]. The resulting diffraction intensities $I_P(\theta_x^1, \theta_y^0)$ and $I_P(\theta_x^1, \theta_y^1)$ of the phase lattices are 9.2% and 8%, respectively. Hence, the probe field is effectively diffracted into the high-order directions, see also Figs. 4(b) and 4(d).

Now we consider the corresponding diffraction pattern of the optically induced lattices in the near-field regime, where the main results are illustrated by Eq. (7). In Figs. 6(a) and 6(b), the near-field Fresnel diffraction patterns in the case of amplitude and phase lattice are compared. Figures 6(a1)–6(a4) show a typical 2D Talbot carpet pattern at four different imaging planes $Z = 0$, $z_T/2$, $2z_T/3$, and z_T. It is obvious that resolution of the diffraction patterns, including transverse and

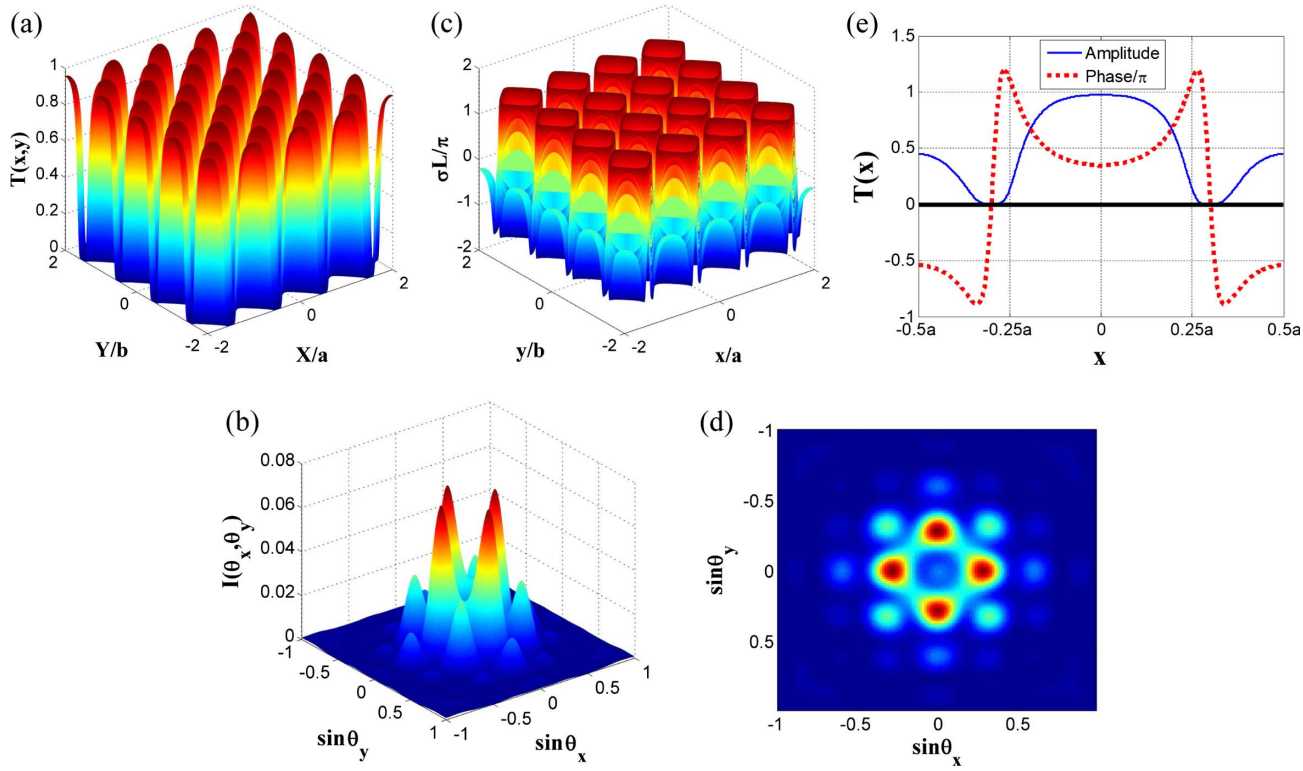

Fig. 4. Phase-type lattice, with settings $\Omega_C = 15$ MHz, $\Delta_1 = 10$ MHz, and $\Delta_2 = 0$ MHz. (a) The amplitude and (b) the phase of the transmission function $T(x, y)$ plotted over four space periods along x and y. (c) The corresponding normalized diffraction intensity $I(\theta_x, \theta_y)$ as a function of sin θ_x and sin θ_y. (d) 2D transverse patterns corresponding to (c). (e) The amplitude (solid curve) and the phase (dashed curve) of the transmission function $T(x, y)$ as a function of x within a single space period. Other parameters are $\gamma_{ab} = 1$ MHz, $\gamma_{ac} = 0.2$ MHz, $a/\lambda_P = b/\lambda_P = 4$, $L = 10$, and $P = Q = 1$.

longitudinal, are identical. The diffraction pattern at $z_T/2$ is shifted laterally by half a period with respect to the imaging at 0, which agrees well with the theoretical prediction as described above. On the other hand, the contrast at those Talbot planes is approximately unity. However, the visibility as well as the signal-to-noise ratio are limited as the phase modulation is absent in C_{mn}. In Figs. 6(b1)–6(b4), the near-field diffraction patterns of phase-type lattice at $Z = 0$, $z_T/2$, $2z_T/3$, and z_T are shown. Evidently, the location of the Talbot plane in this case exactly coincides with the amplitude lattice case. Moreover, the longitudinal resolution of the corresponding diffraction pattern are identical as well. Those properties are independent of the introduced phase modulation. Compared with Fig. 6(a), we noticed that the contrast of the Talbot carpet pattern is reduced slightly at those Talbot planes. However, the visibility and the signal-to-noise

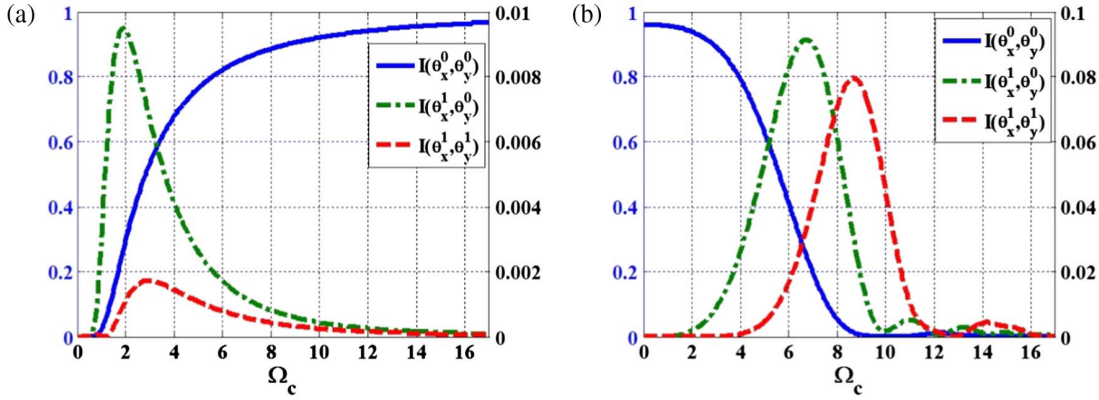

Fig. 5. Normalized diffraction intensity $I_P(\theta_x^0, \theta_y^0)$ (solid line), $I_P(\theta_x^1, \theta_y^0)$ (dashed line), and $I_P(\theta_x^1, \theta_y^1)$ (dashed–dotted line) as a function of Ω_C with (a) amplitude lattice with $\Delta_1 = 0$ MHz, and $\Delta_2 = 0$ MHz and (b) phase-type lattice $\Delta_1 = 10$ MHz, and $\Delta_2 = 0$ MHz. Other parameters are $\gamma_{ab} = 1$ MHz, $\gamma_{ac} = 0.2$ MHz, $a/\lambda_P = b/\lambda_P = 4$, $L = 10$, and $P = Q = 1$.

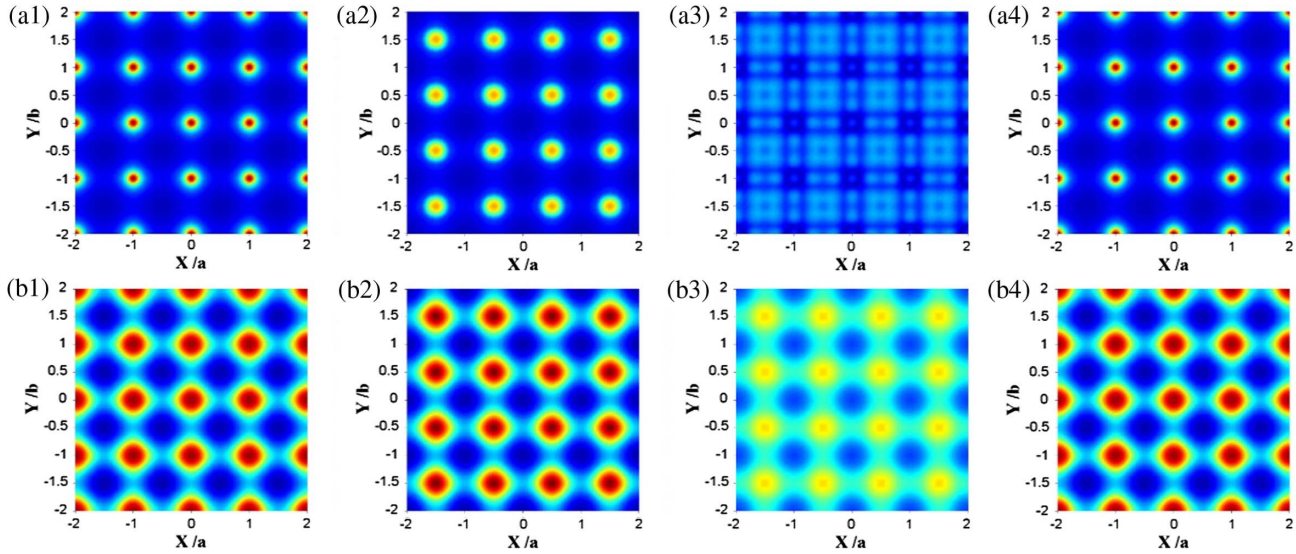

Fig. 6. Near-field diffraction pattern in the case of (a) amplitude-type lattice and (b) phase-type lattice, and (a1)–(a4), (b1)–(b4) Talbot imaging at $Z = 0$, $z_T/2$, $2z_T/3$, and z_T, respectively.

ratio are significantly improved. All of these points agree well with theoretical predictions drawn from Eq. (7) in Section 2.

Indeed, we noticed that the first-order diffraction efficiency of our phase lattices is smaller than the efficiency of an ideal sinusoidal phase grating, which is approximately 34%. However, we know that the diffraction efficiency is very sensitive to the phase modulation, especially cross phase modulation (XPM). Further detailed studies of phase lattice based on XPM will be presented elsewhere.

4. CONCLUSIONS

In summary, we have presented an alternative approach to realizing nonmaterial square lattices in an ultracold atoms ensemble, which is capable of producing a π phase excursion across a weak probe beam with high transmissivity. We demonstrate that the resulting optically induced lattices exert both amplitude and phase modulations on the probe beam in the same way as the hybrid (amplitude and phase) lattices does to the amplitude and phase of an electromagnetic wave. In the far-field regime, we also demonstrate that the atomic ensemble under resonance interaction serves as an amplitude lattice to the probe field, and the medium is close to that of an ideal phase lattice with a predicted diffraction efficiency of 9.2% under the phase modulation condition. In the near-field regime, we address specifically that the phase modulation can be used to improve the quality of Talbot imaging while the contrast of the diffraction pattern is slightly reduced. Such a nonmaterial lattice could find applications in all-optical switching [28–31] at the few photons level. Furthermore, the atomic lattices can be further used as a nondestructive and lensless way to image the ultracold atoms or molecules in the near-field and far-field regimes [32].

Funding. National Natural Science Foundation of China (NSFC) (61605155, 61627812); Fundamental Research Funds for the Central Universities.

Acknowledgment. Feng Wen was partly supported by the 2016 International Postdoctoral Exchange Fellowship Program of the Office of the China Postdoctoral Council.

†These authors contributed equally to this work.

REFERENCES

1. J. D. Joannopoulos, S. G. Johnson, J. N. Winn, and R. D. Meade, *Photonic Crystals: Molding the Flow of Light* (Princeton University, 2011).
2. E. Yablonovitch, "Inhibited spontaneous emission in solid-state physics and electronics," Phys. Rev. Lett. **58**, 2059–2062 (1987).
3. H.-G. Park, S.-H. Kim, S.-H. Kwon, Y.-G. Ju, J.-K. Yang, J.-H. Baek, S.-B. Kim, and Y.-H. Lee, "Electrically driven single-cell photonic crystal laser," Science **305**, 1444–1447 (2004).
4. Y. Akahane, T. Asano, B.-S. Song, and S. Noda, "High-Q photonic nanocavity in a two-dimensional photonic crystal," Nature **425**, 944–947 (2003).
5. C. Denz, S. Flach, and Y. S. Kivshar, *Nonlinearities in Periodic Structures and Metamaterials* (Springer, 2010), Vol. **150**.
6. D. R. Smith, J. B. Pendry, and M. C. Wiltshire, "Metamaterials and negative refractive index," Science **305**, 788–792 (2004).
7. D. Schurig, J. Mock, B. Justice, S. A. Cummer, J. B. Pendry, A. Starr, and D. Smith, "Metamaterial electromagnetic cloak at microwave frequencies," Science **314**, 977–980 (2006).
8. P.-H. Tichit, S. N. Burokur, C.-W. Qiu, and A. de Lustrac, "Experimental verification of isotropic radiation from a coherent dipole source via electric-field-driven LC resonator metamaterials," Phys. Rev. Lett. **111**, 133901 (2013).
9. T. Han, X. Bai, J. T. Thong, B. Li, and C. W. Qiu, "Full control and manipulation of heat signatures: cloaking, camouflage and thermal metamaterials," Adv. Mater. **26**, 1731–1734 (2014).
10. J. D. Joannopoulos, P. R. Villeneuve, and S. Fan, "Photonic crystals: putting a new twist on light," Nature **386**, 143–149 (1997).
11. S. John and J. Wang, "Quantum electrodynamics near a photonic band gap: photon bound states and dressed atoms," Phys. Rev. Lett. **64**, 2418–2421 (1990).
12. A. Alù and N. Engheta, "All optical metamaterial circuit board at the nanoscale," Phys. Rev. Lett. **103**, 143902 (2009).
13. S. F. Mingaleev and Y. S. Kivshar, "Self-trapping and stable localized modes in nonlinear photonic crystals," Phys. Rev. Lett. **86**, 5474–5477 (2001).

14. M. Fleischhauer, A. Imamoglu, and J. P. Marangos, "Electromagnetically induced transparency: optics in coherent media," Rev. Mod. Phys. **77**, 633–673 (2005).
15. H. Y. Ling, Y.-Q. Li, and M. Xiao, "Electromagnetically induced grating: homogeneously broadened medium," Phys. Rev. A **57**, 1338–1344 (1998).
16. M. Mitsunaga and N. Imoto, "Observation of an electromagnetically induced grating in cold sodium atoms," Phys. Rev. A **59**, 4773–4776 (1999).
17. A. W. Brown and M. Xiao, "All-optical switching and routing based on an electromagnetically induced absorption grating," Opt. Lett. **30**, 699–701 (2005).
18. N. Radwell, T. W. Clark, B. Piccirillo, S. M. Barnett, and S. Franke-Arnold, "Spatially dependent electromagnetically induced transparency," Phys. Rev. Lett. **114**, 123603 (2015).
19. A. Andre and M. Lukin, "Manipulating light pulses via dynamically controlled photonic band gap," Phys. Rev. Lett. **89**, 143602 (2002).
20. M. Bajcsy, A. S. Zibrov, and M. D. Lukin, "Stationary pulses of light in an atomic medium," Nature **426**, 638–641 (2003).
21. G. Cardoso and J. Tabosa, "Electromagnetically induced gratings in a degenerate open two-level system," Phys. Rev. A **65**, 033803 (2002).
22. P.-W. Zhai, X.-M. Su, and J.-Y. Gao, "Optical bistability in electromagnetically induced grating," Phys. Lett. A **289**, 27–33 (2001).
23. J. Wen, Y.-H. Zhai, S. Du, and M. Xiao, "Engineering biphoton wave packets with an electromagnetically induced grating," Phys. Rev. A **82**, 043814 (2010).
24. L. Zhao, W. Duan, and S. Yelin, "All-optical beam control with high speed using image-induced blazed gratings in coherent media," Phys. Rev. A **82**, 013809 (2010).
25. D. A. Steck, http://steck.us/alkalidata.
26. J. W. Goodman, *Introduction to Fourier Optics* (Roberts & Company, 2005).
27. F. Zhou, Y. Qi, H. Sun, D. Chen, J. Yang, Y. Niu, and S. Gong, "Electromagnetically induced grating in asymmetric quantum wells via Fano interference," Opt. Express **21**, 12249–12259 (2013).
28. S. Chen, L. Miao, X. Chen, Y. Chen, C. Zhao, S. Datta, Y. Li, Q. Bao, H. Zhang, and Y. Liu, "Few-layer topological insulator for all-optical signal processing using the nonlinear Kerr effect," Adv. Opt. Mater. **3**, 1769–1778 (2015).
29. H. Wu, J. Tang, Z. Yu, J. Yi, S. Chen, J. Xiao, C. Zhao, Y. Li, L. Chen, and S. Wen, "Electrically optical phase controlling for millimeter wave orbital angular momentum multi-modulation communication," Opt. Commun. **393**, 49–55 (2017).
30. F. Wen, I. Ali, A. Hasan, C. Li, H. Tang, Y. Zhang, and Y. Zhang, "Ultrafast optical transistor and router of multi-order fluorescence and spontaneous parametric four-wave mixing in Pr^{3+}:YSO," Opt. Lett. **40**, 4599–4602 (2015).
31. Y. Q. Zhang, Y. V. Kartashov, F. Li, Z. Y. Zhang, Y. P. Zhang, M. R. Belić, and M. Xiao, "Edge states in dynamical superlattices," ACS Photon. **4**, 2250–2256 (2017).
32. C. Stehle, H. Bender, C. Zimmermann, D. Kern, M. Fleischer, and S. Slama, "Plasmonically tailored micropotentials for ultracold atoms," Nat. Photonics **5**, 494–498 (2011).